

Complementary imaging of the nuclear dynamics in laser-excited diatomic molecular ions in the time and frequency domains

This content has been downloaded from IOPscience. Please scroll down to see the full text.

2014 J. Phys. B: At. Mol. Opt. Phys. 47 124003

(<http://iopscience.iop.org/0953-4075/47/12/124003>)

View [the table of contents for this issue](#), or go to the [journal homepage](#) for more

Download details:

This content was downloaded by: thummuwe

IP Address: 129.130.106.65

This content was downloaded on 10/06/2014 at 19:29

Please note that [terms and conditions apply](#).

Review Article

Complementary imaging of the nuclear dynamics in laser-excited diatomic molecular ions in the time and frequency domains

M Magrakvelidze¹, A Kramer², K Bartschat² and U Thumm¹¹ J.R. Macdonald Laboratory, Department of Physics, Kansas State University, Manhattan, KS 66506, USA² Department of Physics and Astronomy, Drake University, Des Moines, IA 50311, USAE-mail: thumm@phys.ksu.edu

Received 12 December 2013, revised 14 February 2014

Accepted for publication 21 February 2014

Published 10 June 2014

Abstract

Experimentally, the bound and dissociative nuclear dynamics in small molecular ions can be resolved in time by using intense ultrashort pump in combination with delayed probe laser pulses. We discuss the modelling of related pump–probe-delay-dependent fragment kinetic-energy-release (KER) spectra for the laser-induced dissociative ionization of selected diatomic molecules and show how the quantum-mechanical simulation of measured KER spectra—in both the time domain and as a function of the beat frequency between molecular vibrational levels—reveals dissociation pathways and the characteristics of initially occupied molecular potential curves.

Keywords: kinetic energy release, molecular dynamics, pump–probe, molecular ion, diatomic molecule, quantum beat, strong field physics

(Some figures may appear in colour only in the online journal)

1. Introduction

Over the past decades, advances in laser technology in generating ultrashort and intense laser pulses have enabled the time-resolved imaging of the nuclear wave-packet dynamics of diatomic molecules by employing intense pump and probe laser pulses with pulse durations that are significantly shorter than the molecular vibration period [1–5]. In particular, the dynamics of the wave-packet motion for processes such as dissociation and Coulomb explosion are investigated experimentally and theoretically by analysing kinetic-energy-release (KER) spectra as functions of the adjustable pump–probe delay in both the smallest diatomic molecules, H₂ and D₂ [3–8], as well as in heavier diatomic molecules, such as O₂, N₂, CO [9–12], and noble-gas dimers [13, 14]. More recently, these time-resolved investigations of the nuclear

dynamics in small molecules were extended from the infrared (IR) spectral range to the extreme ultraviolet (XUV) domain in XUV-pump–XUV-probe experiments at free-electron laser facilities [15–17].

In a typical pump–probe experiment the pump pulse ionizes the neutral molecule while a delayed probe pulse dissociates the molecular ion, thereby revealing the nuclear dynamics in the bound and dissociating molecular ions in KER spectra. For instance, immediately following the single ionization of a D₂ molecule in an intense few femtosecond (fs) pump pulse, a nuclear vibrational wave packet is launched and propagated in the lowest $1\sigma_g$ adiabatic potential curve of the molecular ion (figure 1). Experimentally, the KER spectrum is measured as a function of the pump–probe delay, from which the internuclear distance (R)-dependent probability density of the vibrational wave packet can be reconstructed by

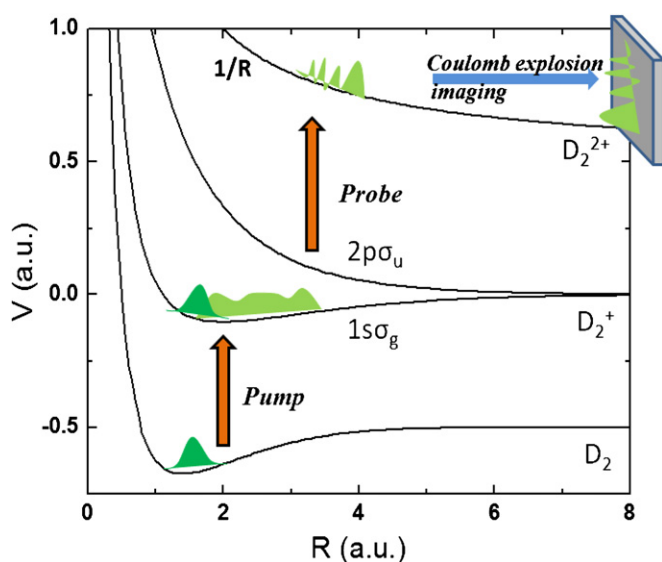


Figure 1. Schematic of the pump–probe process allowing for the time-resolved detection of the nuclear dynamics in deuterium molecular ions. The pump-laser pulse launches a nuclear vibrational wave packet from the electronic and vibrational ground state of the neutral molecule onto the D_2^+ ($1s\sigma_g$) potential curve by ionizing D_2 and starts the molecular clock. After a variable time delay, an intense short probe pulse can cause fragmentation by Coulomb explosion, leading to fragmentation along the repulsive $1/R$ Coulomb potential curve and allowing for the detection of the fragment kinetic energy distribution.

‘Coulomb-explosion imaging’ [7, 18]. The vibrational wave packet can be described as a coherent superposition of stationary vibrational states in the $1s\sigma_g$ adiabatic potential of the molecular cation, which dephase over time due to the anharmonicity of the potential curve [5, 19, 20]. This collapse of the wave packet is followed by full and partial revivals at the revival period T_{rev} and at fractions of T_{rev} [21], respectively. At these revivals, the localized periodic motion of the wave packet reemerges as the stationary vibrational states interfere in such a way that either their original relative phases in the initially localized wave packet are approximately restored (full revivals) or a fraction of the original relative phases is restored (partial revivals). For heavier molecules, such as O_2 , a large number of adiabatic potential curves of the molecular ion can typically be populated in the initial ionization by the pump pulse. Consequently, tracing adiabatic states that are involved in the pump-laser-induced nuclear dynamics in heavier molecular ions is significantly more complicated than in H_2^+ (and its isotopes). A noticeable exception, however, is found in the weakly (van-der-Waals) bound noble-gas dimers. Here, single ionization by the pump pulse results in molecular ions with a comparatively simple electronic structure consisting of either four (not including fine structure) or six (including fine structure) adiabatic states [13, 14].

In this paper we review the time-resolved imaging of the nuclear dynamics in diatomic molecules as a function of the pump–probe delay in comparison with an alternative and complementary analysis of the same basic KER spectra. The alternative analysis is based on the Fourier

transformation of the time- and internuclear-separation-dependent wavefunction probability density or, equivalently, on the Fourier transformation of the delay-dependent KER spectra. This frequency-domain analysis allows for the extraction of the distribution of stationary vibrational states and the mapping of the nuclear potential curves of the molecular cation [5, 7, 8]. The method was applied in dissociative ionization calculations for the D_2^+ molecule [5–8] and later extended to heavier molecules [10, 11]. It was validated in a proof-of-principles experiment for D_2^+ [5].

Throughout this publication we neglect molecular rotation and discuss numerical models that assume molecular alignment along the polarization direction of linearly polarized laser pulses. The neglect of molecular rotation is justified if the delay between pump and probe pulse is significantly shorter than the rotational period T_{rot} of the parent molecule and molecular ion [1–5, 9, 10, 12–16, 20]. The assumption of molecular alignment is valid, even though the gaseous target molecules are randomly oriented in the vast majority of pump–probe experiments performed to date, as the coincident detection of molecular fragments allows for the ‘post selection’ after laser-induced dissociation of a subset of aligned molecules. For pump–probe delays that are of the order of or larger than T_{rot} , the vibrational and rotational molecular dynamics needs to be taken into account. For the modelling and interpretation of ro-vibrational KER spectra we refer to [6].

We first briefly review the modelling and analysis of KER spectra in the time domain (section 2.1) and then supplement the discussion of pump–probe-delay-dependent KER spectra by their analysis in the frequency domain (section 2.2). In section 3 we discuss numerical examples for the nuclear vibrational motion in D_2^+ , O_2^+ , and noble-gas dimer molecular ions in the time and frequency domains and relate characteristic features that are best identified in either one or the other domain to measured KER spectra. We conclude with a brief summary and outlook in section 4. We use atomic units (au) throughout this work unless indicated otherwise.

2. Modelling the laser-induced nuclear dynamics and KER spectra

2.1. Time-domain analysis

We model the nuclear dynamics in the pump–probe sequence (figure 1), where the pump pulse ionizes the neutral diatomic molecules and a delayed probe pulse destructively images the nuclear motion in the molecular ion. We assume a delay τ between the temporal centres of the two pulses. The laser electric field is modelled as a cosine wave within a Gaussian envelope and is linearly polarized along the internuclear axis. In all numerical results discussed in section 3 we assume that the neutral diatomic molecules were singly ionized by an intense short laser pulse. We approximate the quantum states of the resulting molecular ion as adiabatic Born–Oppenheimer (BO) states and truncate the BO expansion. We outline our numerical model by including only the lowest and the first

excited adiabatic state. However, the following description can easily be extended to include more than two terms in the BO expansion. Neglecting molecular rotation, the wavefunction of the diatomic molecular ion is then given by

$$\Phi(\vec{r}, R; t) = \frac{1}{\sqrt{2}}[\Psi_1(R, t)\chi_1(\vec{r}, R, t) + \Psi_2(R, t)\chi_2(\vec{r}, R, t)], \quad (1)$$

where Ψ_1 and Ψ_2 are nuclear wavefunctions, χ_1 and χ_2 the ground and first excited BO electronic states, and \vec{r} collectively denotes all electronic position vectors. For the simplest molecular ion, H_2^+ , the indices 1 and 2 correspond to the adiabatic states $1s\sigma_g$ and $2p\sigma_u$.

We write the ground-state component of the initial nuclear vibrational wave packet as a superposition of stationary vibrational eigenstates $\{\phi_\mu\}$ in the electronic ground-state potential $V_1(R)$, with (in general complex) amplitudes $\{a_\mu\}$ and assume that the excited state component is initially not occupied,

$$\Psi_1(R, 0) = \sum_{\mu} a_{\mu} \phi_{\mu}(R), \quad \Psi_2(R, 0) = 0. \quad (2)$$

The most elementary way to model the ionization process assumes instant ionization of the neutral parent molecule and employs real-valued amplitudes $\{a_\mu\}$ in the Franck–Condon (FC) approximation [7, 8, 22]. The FC amplitudes $\{a_\mu\}$ can be obtained numerically by imaginary-time propagation of a trial function on the ground-state BO potential curve of the neutral molecule to generate the ground-state wavefunction $\Psi_0(R, t=0)$ of the neutral parent molecule, followed by projection onto stationary vibrational states of the molecular ion, $\{a_\mu = \langle \phi_\mu | \Psi_0(R, t=0) \rangle\}$. A more realistic and laser-pulse-parameter-dependent approximation for modelling the initial ionization of the neutral molecule is based on molecular Ammosov–Delone–Krainov (ADK) ionization rates (see [13] for details).

The bound and dissociating nuclear motion of the molecular ion can be described by projecting the time-dependent Schrödinger equation on the adiabatic electronic states χ_1 and χ_2 . For electronic states χ_1 and χ_2 with well-defined parity this leads to coupled equations

$$i \frac{\partial}{\partial t} \begin{pmatrix} \Psi_1(R, t) \\ \Psi_2(R, t) \end{pmatrix} = \begin{pmatrix} T_R + V_1(R) & d_{12}(R)E(t - \tau) \\ d_{12}(R)E(t - \tau) & T_R + V_2(R) \end{pmatrix} \times \begin{pmatrix} \Psi_1(R, t) \\ \Psi_2(R, t) \end{pmatrix} \quad (3)$$

for the time evolution of the nuclear wavefunction components, where μ is the reduced mass of the nuclei, $T_R = -\frac{1}{2\mu} \frac{\partial^2}{\partial R^2}$ is the nuclear kinetic energy operator, and $V_1(R)$ and $V_2(R)$ denote the lowest two BO potential curves of the molecular ion. The dipole coupling between the two adiabatic electronic states in the presence of laser fields is defined as $d_{12} = \langle \Psi_1 | \vec{r} | \Psi_2 \rangle$. We numerically solve equation (3) using the Crank–Nicolson finite-difference method [8, 23].

Prior to the pump pulse, the two states in equation (3) are decoupled, and the nuclear wavefunction Ψ_1 evolves as a bound nuclear wave packet on the adiabatic potential curve V_1 , undergoing characteristic cycles of dephasing and revival [8, 18]. The amplitudes $\{a_\mu\}$ in equation (2) remain

time-independent between the assumed instantaneous initial ionization by the pump pulse at $t=0$ and the onset of the probe pulse [7]. During this time interval, the nuclear probability density can be written as

$$\rho(R, t) = \int dr |\Phi(\vec{r}, R; t)|^2 = |\Psi_1(R, t)|^2 + |\Psi_2(R, t)|^2 \\ = \sum_{\mu} |a_{\mu}|^2 |\phi_{\mu}(R)|^2 + \sum_{\mu \neq \nu} a_{\mu}^* a_{\nu} e^{-i(E_{\nu} - E_{\mu})t} \phi_{\mu}^*(R) \phi_{\nu}(R). \quad (4)$$

The diagonal term (first term in the second line) is time independent and gives a large incoherent background to the wavefunction probability density. We subtract this diagonal contribution from the probability density to eliminate the dominant incoherent static terms in equation (4).

2.2. Frequency-domain analysis

Quantum-beat (QB) spectra (also referred to as ‘power spectra’) are obtained by Fourier transforming the nuclear probability density as a function of the propagation time, separately for each internuclear distance R . Each of the QB frequencies can be linked to the contributing vibrational energy levels of the potential curve, and the derivative of the molecular potential energy curve can be mapped from the power spectra [8].

We Fourier transform the coherent (time-dependent) terms in equation (4) over the finite time T and take the square of the result to obtain the power spectrum

$$P(R, \omega; T) = \left| \sum_{\mu, \nu=0}^N a_{\mu}^* a_{\nu} \phi_{\mu}^*(R) \phi_{\nu}(R) \delta_T(\Delta\omega_{\mu, \nu} - \omega) \right|^2, \quad (5)$$

where the broadened δ -function is defined as

$$\delta_T(\Omega) \equiv \frac{1}{2\pi} \int_0^T dt e^{i\Omega t} = \frac{1}{\pi} e^{i\Omega T/2} \frac{\sin(\Omega T/2)}{\Omega} \quad (6)$$

and centred at the QB energies $\Delta\omega_{\mu, \nu} = \omega_{\nu} - \omega_{\mu}$. It is broadened due to the Fourier transformation over a *finite* time interval. Equation (6) applies to free propagation of the nuclear vibrational wave packet only. If the action of the probe laser pulse is to be included, the power spectrum must be calculated numerically and the maximal time T is associated with the interval over which pump–probe delays are sampled. In the limit of large sampling times, δ_T becomes identical to the usual Dirac δ -function, and the power spectrum $P(R, \omega; \infty)$ reproduces the QB spectrum at infinite resolution. Further details on the properties and interpretation of $P(R, \omega; T)$ can be found in [8].

For simulating the KER spectra, we numerically propagate the coupled equations (3) for a sufficiently long time T (several hundreds of fs up to a few ps), including the field-free propagation of the nuclear wave packets after the action of the probe pulse. This allows us to separate the bound and dissociating parts of the nuclear motion by selecting an internuclear cutoff distance R_1 that provides an effective range for the bound nuclear motion. The bound motion of the wave packet remains restricted to distances $R < R_1$, while the probability current associated with the dissociation of the

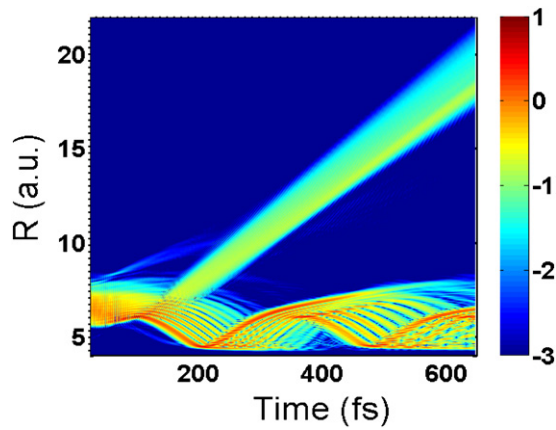


Figure 2. Probability density $\rho(R, t)$ (logarithmic colour/greyscale) for a two-state calculation including the $I(1/2)_u$ and $II(1/2)_g$ states of Kr_2^+ dipole-coupled at the fixed pump–probe delay $\tau = 140$ fs in the electric field of a 60 fs, 10^{14} W cm^{-2} , 800 nm probe pulse.

molecular ion is associated with $R > R_1$. As an example, figure 2 shows the probability density of Kr_2^+ in a 60 fs (FWHM in field strength), 10^{14} W cm^{-2} , 800 nm field, at a fixed pump–probe pulse delay of $\tau = 140$ fs [14]. The bound and dissociative portions of the wave packet are clearly visible, and a cutoff distance of $R_1 = 10$ is suitable. In calculating KER spectra, we ensure that our numerical results are stable with regard to variations of R_1 over a reasonable range of distances and converged in all numerical parameters (numerical grid size R_{max} , equidistant grid spacing ΔR , and number of equidistant time steps Δt). The numerical parameters for the nuclear wave-packet evolution shown in figure 2 are $R_{\text{max}} = 100$, $\Delta R = 0.01$, and $\Delta t = 1$.

Fourier transformation of the dissociating portions of the nuclear wave packets over the interval $[R_1, R_{\text{max}}]$ yields the momentum representations of the dissociating wave packets [10, 11]

$$\tilde{\Psi}_i^{\text{diss}}(P, T) = \int_{R_1}^{R_{\text{max}}} dR \Psi_i^{\text{diss}}(R, T) e^{-iPR}, \quad i = 1, 2. \quad (7)$$

The distribution of fragment KERs is now given by

$$C^{\text{diss}}(E, \tau) \propto |\tilde{\Psi}_1^{\text{diss}}(P, T)|^2 + |\tilde{\Psi}_2^{\text{diss}}(P, T)|^2, \quad (8)$$

where $E = \frac{P^2}{2M}$ is the kinetic energy per fragment. After subtracting the large incoherent static contribution

$$C_{\text{incoh}}^{\text{diss}}(E) = \frac{1}{T} \int_0^T d\tau C^{\text{diss}}(E, \tau) \quad (9)$$

from C^{diss} , we obtain the power spectrum as a function of the QB frequency $f = \omega/2\pi$,

$$P^{\text{diss}}(E, f) = \left| \int_0^T d\tau C_{\text{coh}}^{\text{diss}}(E, \tau) e^{-i2\pi f\tau} \right|^2. \quad (10)$$

Example power spectra for various diatomic molecules will be discussed in section 3 below. These examples are based on ‘snapshots’ of the nuclear probability density equation (4) taken at time $t = \tau + 50$ fs, i.e. 50 fs after the end of the Gaussian probe pulse. In numerical tests, we found that further increasing the propagation time does not noticeably change the numerical results discussed in this publication.

We note that the ‘virtual detector’ (VD) method is an efficient alternative computational scheme for extracting momentum distributions from numerical position-space wavefunctions without propagating the wave packet over a large numerical grid. This method consists in calculating momentum expectation values of the fragment momenta over a small position-space interval at the edge of the numerical grid at every time step and combines fragment momenta that fall into small momentum bins into a histogram. This histogram is then converted into a KER spectrum [11, 24]. For all numerical examples shown below, the two methods, equation (10) and the VD approach, provide indistinguishable results on the graph shown in this work.

3. Numerical results for the nuclear dynamics and KER spectra

In this section, we discuss probability densities, power spectra, and nuclear KER spectra for selected diatomic molecules in the strong laser fields.

3.1. D_2 molecules

Starting with the simple molecular ion D_2^+ , we present the wave-packet evolution on the $1s\sigma_g$ adiabatic potential curve in the time and frequency domains. The anharmonicity of the potential curve causes the wave packet to dephase. This dephasing is followed by periodic wavefunction revivals [10, 21]. Features of this vibrational revival phenomenon give information about the energetic spacing and nodal structure of the relevant vibrational levels, the initial wave packet, and the nuclear vibrational dynamics. Figure 3 shows probability densities as a function of propagation time and internuclear distance R , along with the corresponding power spectra. The vibrational oscillation period in D_2^+ is about 20 fs and the full revival time is approximately 590 fs (figure 3(a)). The power spectrum in figure 3(b) shows distinct quantum beats below 50 THz. Each vertical ‘QB line’ has a nodal structure along the R axis that reveals the combined nodal structure of the two beating vibrational levels (cf equation (5)). For example, the quantum-beat frequency line at 47 THz has one node, indicating beating between the first and second vibrational eigenstates in the $1s\sigma_g$ adiabatic electronic state of D_2^+ . In addition, the contour of the $1s\sigma_g$ potential curve (more accurately stated, of the derivative of the $1s\sigma_g$ potential curve [8]) is clearly visible in the power spectrum (figure 3(b)). The large yields in figure 3(b) with the closest spacing in QB frequencies extending up to about 48 THz correspond to QBs between successive vibrational levels ν and $\nu+1$. The sequence of fainter lines separated by about twice the frequency of the $(\nu, \nu+1)$ series of vertical lines is due to QBs between the next nearest vibration levels ν and $\nu+2$. The faintest vertical lines correspond to the $(\nu, \nu+3)$ and higher QB series.

The ‘Floquet picture’ is commonly used for explaining molecular dynamics in laser pulses [23, 25]. In this picture, due to the presence of an oscillating electric field, eigenstates of the free molecule evolve as so-called field-dressed states (figure 4(a)). These field-dressed states are separated

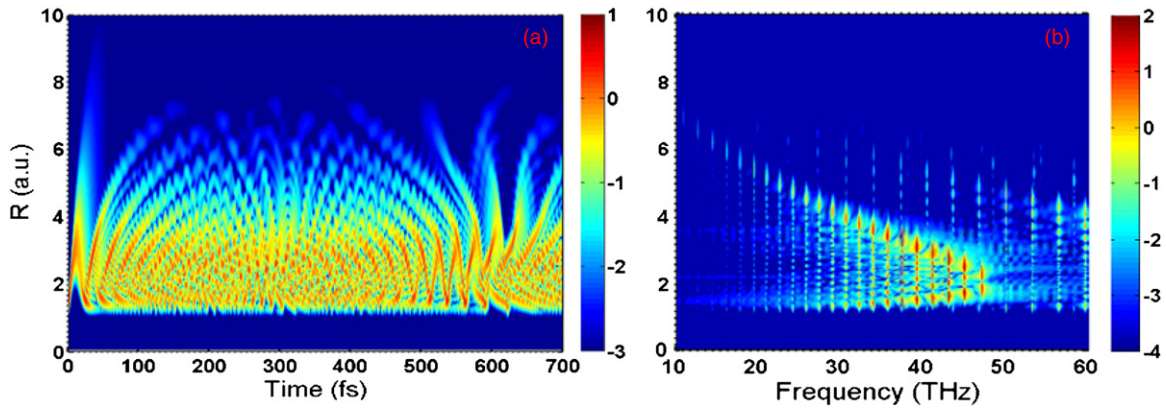


Figure 3. (a) Evolution of the nuclear probability density and (b) power spectrum (logarithmic colour/greyscale) for field-free propagation of the D_2^+ molecular ion on the $1s\sigma_g$ adiabatic potential curve.

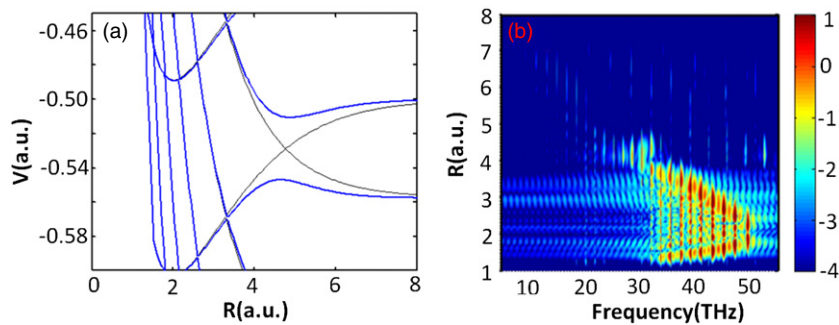


Figure 4. (a) Field-dressed adiabatic potential curves ($1s\sigma_g$ and $2p\sigma_u$) for the D_2^+ molecular ion in an 800 nm, $10^{13} \text{ W cm}^{-2}$, 20 fs probe laser pulse. The adiabatic potential curves are adapted as described in footnote ³. (b) Power spectrum (logarithmic colour/greyscale) of the field-dressed molecular ion for a delay range of $T = 5$ ps.

energetically by a photon energy (thin black lines in figure 4(a) corresponding to one-photon field-dressed states). Coupling of the nuclear motion and the electric field leads to avoided crossings of Floquet states. Avoided crossings of the $1s\sigma_g$ and $2p\sigma_u$ states of D_2^+ are separated by an odd number of photons ($1\omega, 3\omega, \dots$), due to parity conservation (thick blue lines in figure 4(a)). Depending on the laser intensity, the more energetic upper field-dressed potential curve may form a potential well near the avoided crossing point in which molecular probability density can be trapped. This ‘bond-hardening (BH) well’ changes its shape with increasing laser intensity and is centred at the internuclear distance $R = 4.8$ in the power spectra in figures 4(a) and (b). This spectrum is calculated for 20 fs, 800 nm, $10^{13} \text{ W cm}^{-2}$ peak intensity probe pulses and distorted compared to the field-free spectrum in figure 3(b). It maps the field-dressed $1s\sigma_g$ and $2p\sigma_u$ potential curves. Several features, including bond softening (BS) below the avoided crossing and BH [7, 26], can be recognized and were studied for different probe-laser parameters in [7].

Figure 5 summarizes the measured and calculated proton energy as a function of the pump–probe delay in the dissociation process $D_2^+ \rightarrow D^+ + D$ and corresponding power spectra. The measured wave-packet oscillation period of ~ 20 fs in the $1s\sigma_g$ state and revival time of ~ 580 fs in figure 5(a) are reproduced in the calculation (figure 5(c)). A fractional revival is visible near delays of 290 fs. The

monotonously decreasing line in figure 5(a) starting at 2 eV and ~ 40 fs delay is due to ‘delayed dissociation’ [20], i.e. partial dissociative ionization by the pump pulse followed by ionization of the remaining bound part of the wave packet by the probe pulse. This process is not included in the simulated KERs in figure 5(c). Power spectra for the dissociation of D_2^+ are shown in figures 5(b) and (d) as functions of the internuclear distance R and the QB frequency for 10 fs, 800 nm, $3 \times 10^{14} \text{ W cm}^{-2}$ laser pulses [5].

The inset in figure 5(b) displays the measured temporal profile of the pump and probe pulses used in the experiment. The superimposed white contour lines in figure 5(b) show numerical results that were computed for this experimental probe-pulse profile. The oscillation periods and revival times calculated in figure 5(c) without including the probe pulse agree with the measured values in figure 5(a). The comparison of the power spectra in figures 4(b) and 5(b) reveals similar QB frequencies for the propagation of the D_2^+ nuclear wave packet with and without the presence of the probe laser pulse. This allows us to use parameters extracted from field-free propagation calculations as a guide for the analysis of measured spectra, in order to identify transient adiabatic states relevant to the dynamics of diatomic molecular ions with a large number of adiabatic electronic states.

3.2. O_2 molecules

For heavier diatomic molecules such as O_2^+ , the vibrational nuclear dynamics is more complicated than in D_2^+ due

³ References for adiabatic potential curves and dipole coupling elements of noble gas dimers are given in [13].

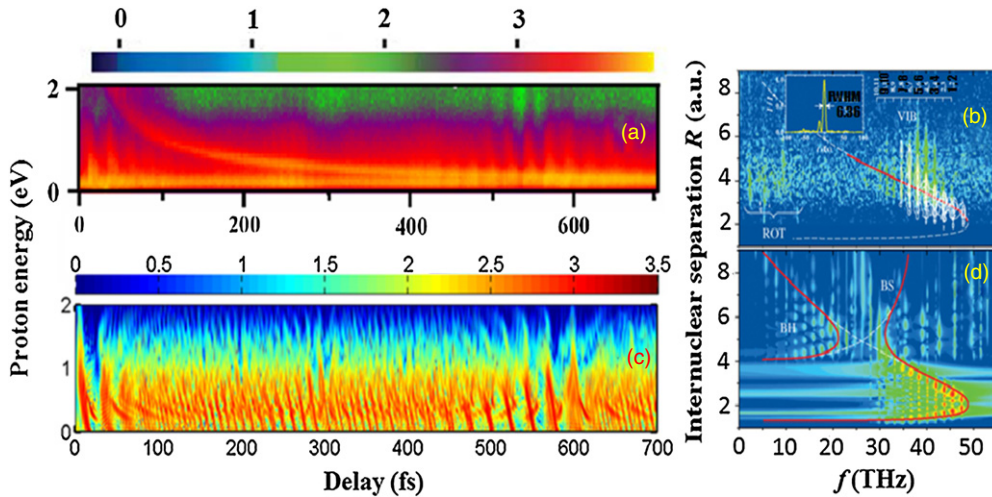


Figure 5. (a) Measured [20] and (c) calculated deuteron KER spectrum (in logarithmic colour/greyscales) as a function of the pump–probe delay for $D_2^+ \rightarrow D^+ + D$ dissociation for 10 fs, 800 nm 3×10^{14} W cm $^{-2}$ peak intensity Gaussian probe pulses. (b) Measured and (d) calculated power spectrum for 50 fs, 800 nm, 10^{14} W cm $^{-2}$ probe pulses. The calculated spectrum in (d) includes a 50 fs 10^{13} W cm $^{-2}$ peak intensity Gaussian probe-pulse pedestal and is obtained by propagating the nuclear wave packet to the centre. The superimposed white contour lines in (b) show numerical results based on the experimental pulse profile shown in the inset. Solid red and dashed white superimposed lines in (b), (d) are meant to guide the eye and retrace the contours of (b) field-free and (d) laser-dressed molecular potential curves, showing evidence for BH and BS. The results in (b), (d) are given on a logarithmic colour/greyscale covering three orders of magnitude. (b), (d) are adapted with permission from [5]. © 2007, American Physical Society.

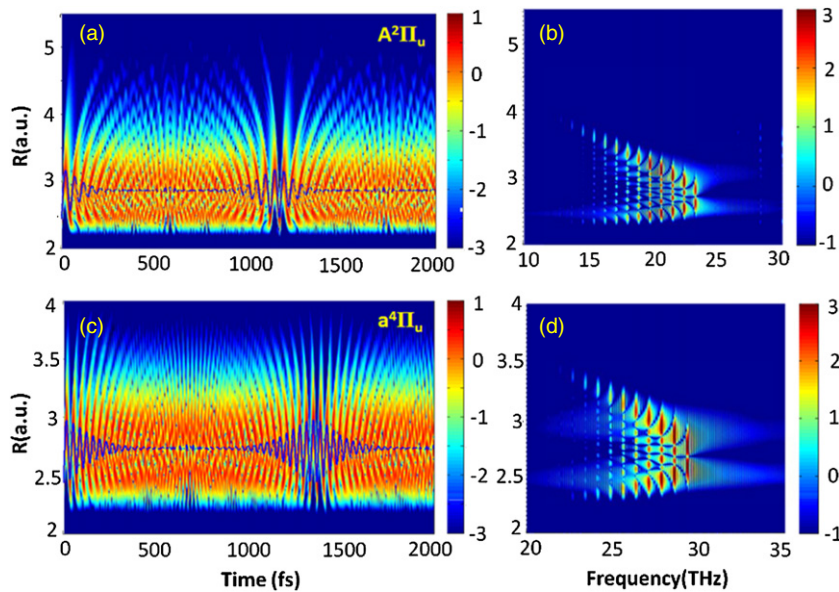


Figure 6. (a), (c) Nuclear probability density and (b), (d) corresponding power spectra $P(R, \omega, t)$ (logarithmic colour/greyscales) for wave-packet propagation in the (a), (b) $A^2\Pi_u$ and (c), (d) $a^4\Pi_u$ adiabatic states of the O_2^+ molecular ion for a maximum propagation time of 7 ps.

to the presence of many adiabatic states that might be intermittently populated during the dissociative ionization. Figure 6 shows probability densities and power spectra for field-free propagation on the $A^2\Pi_u$ and $a^4\Pi_u$ states of O_2^+ as an example. The oscillation periods (36 fs for the $A^2\Pi_u$ and 34 fs for the $a^4\Pi_u$ state) and revival times (1.2 ps for the $A^2\Pi_u$ and 1.4 ps for the $a^4\Pi_u$ state, respectively) extracted from these calculations can be used as a guide for identifying relevant adiabatic states involved in the nuclear dynamics after comparing them to the measured values [9–11]. Again, as for D_2^+ , the power spectra for O_2^+ show QB frequencies. These

frequencies and the R -dependent nodal structure reveal pairs of beating vibrational eigenstates within the given adiabatic state of the molecular ion. The field-free adiabatic potential curves $A^2\Pi_u$ and $a^4\Pi_u$ of O_2^+ can be deduced from the power spectra.

Figure 7 summarizes the power spectra for different laser-field parameters and corresponding field-free (thin black) and field-dressed (thick blue lines) $a^4\Pi_u$ and $f^4\Pi_g$ potential curves of O_2^+ . The FC regions are indicated as green shaded areas, and the red horizontal lines correspond to the FC probabilities $\{|a_\mu|^2\}$. The $a^4\Pi_u$ state, dipole-coupled to the $f^4\Pi_g$ state,

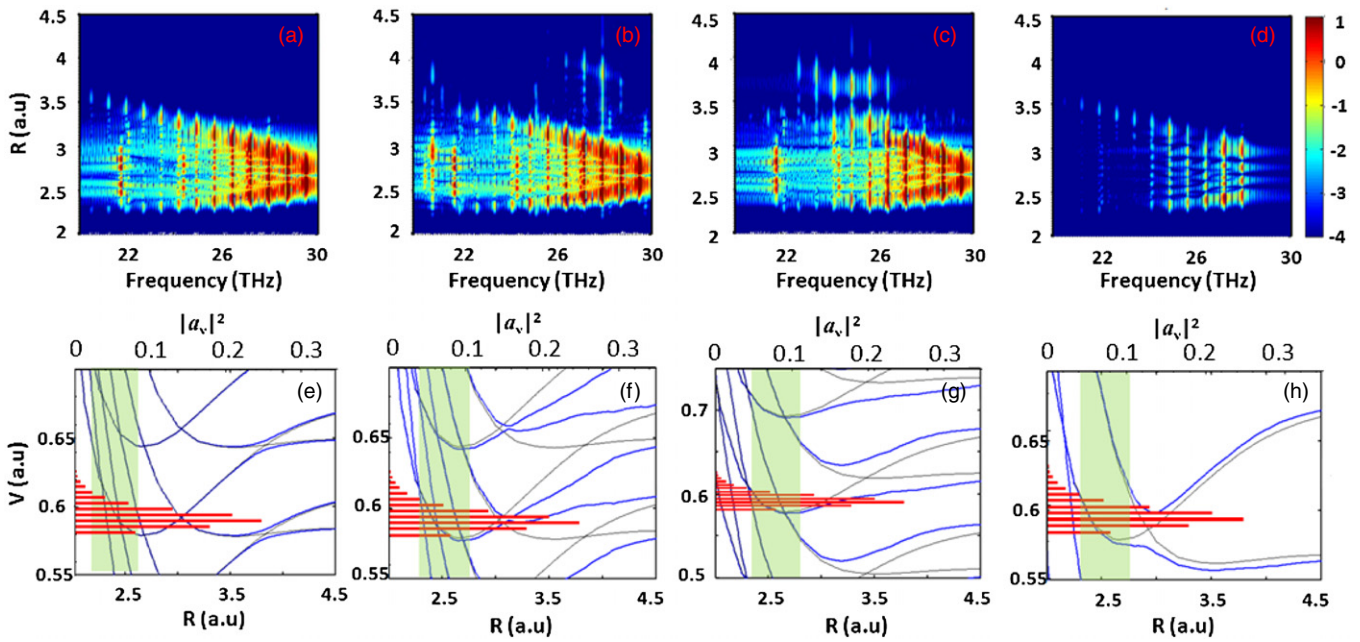


Figure 7. (a)–(d) Power spectra from calculations simulating the propagation of vibrational wave packets in the $a^4\Pi_u$ and $f^4\Pi_g$ adiabatic states of the O_2^+ molecular ion (logarithmic colour/greyscale) that are dipole-coupled by the electric field of the probe pulse. The probe pulses have a length of 20 fs (FWHM in field strength), wavelengths (a), (b) 1400 nm, (c) 800 nm, (d) 400 nm, and peak intensities (a) 10^{12} W cm $^{-2}$, (b), (c), (d) 10^{14} W cm $^{-2}$. The delay range T covers 12 ps. (e)–(h) Corresponding field-dressed adiabatic potentials, based on adiabatic potential curves and dipole coupling elements from the footnote (see footnote 3). Green shaded areas indicate the FC region, and the red horizontal lines correspond to the FC probabilities $\{|a_\mu|^2\}$ at the corresponding stationary vibrational-state energies $\{\omega_\mu\}$.

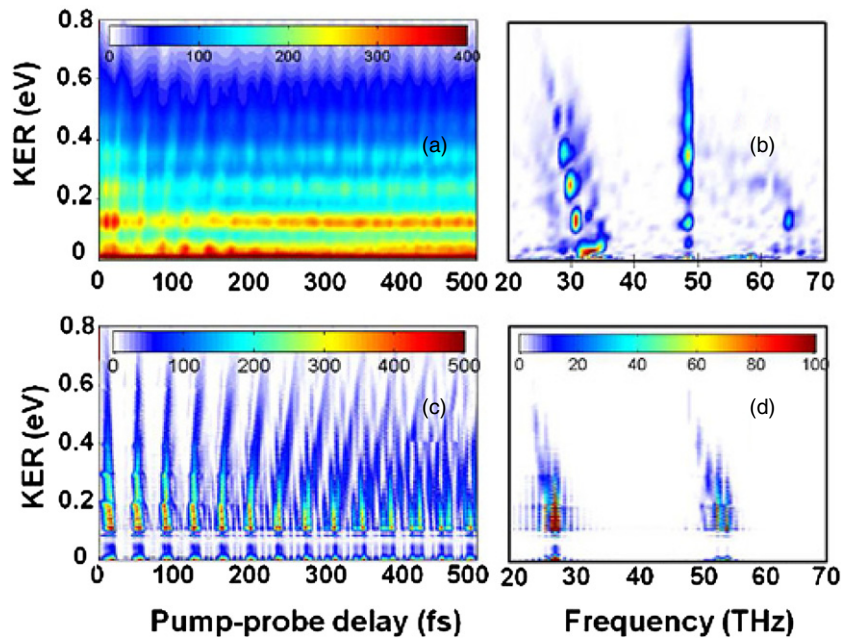


Figure 8. (a) (b) Measured [10, 11] and (c), (d) calculated KER spectra for $O_2^+ \rightarrow O^+ + O$ dissociation in 10 fs 800 nm, 4×10^{14} W cm $^{-2}$ peak intensity laser pulses. The calculated KERs in (c), (d) include a 100 fs, 800 nm, 5×10^{11} W cm $^{-2}$ peak intensity Gaussian pedestal. (a), (c) KERs as a function of the pump–probe delay. (b), (d) Corresponding power spectra (propagated 800 fs past the Gaussian 10 fs pulse) for a delay range of $T = 2$ ps. Adapted with permission from [10]. © 2011, American Physical Society.

results in power spectra that are quite different for all of the cases shown.

The effects of the probe-pulse electric field on the molecular potential curve become clear by comparing figures 7(a) and (b). As the pulse intensity increases, the dressed potential curves widen. This effect is further enhanced

by increasing the pulse frequency in figures 7(c) and (d). For different photon energies and peak intensities, the 1ω crossings of the $f^4\Pi_g$ and $a^4\Pi_u$ states occur at different internuclear distances, and the corresponding BH wells are located at different internuclear distances $R = 3.5$ (figure 7(e)), 3.1 (figure 7(f)), 3.2 (figure 7(g)), and 3.0 (figure 7(h)).

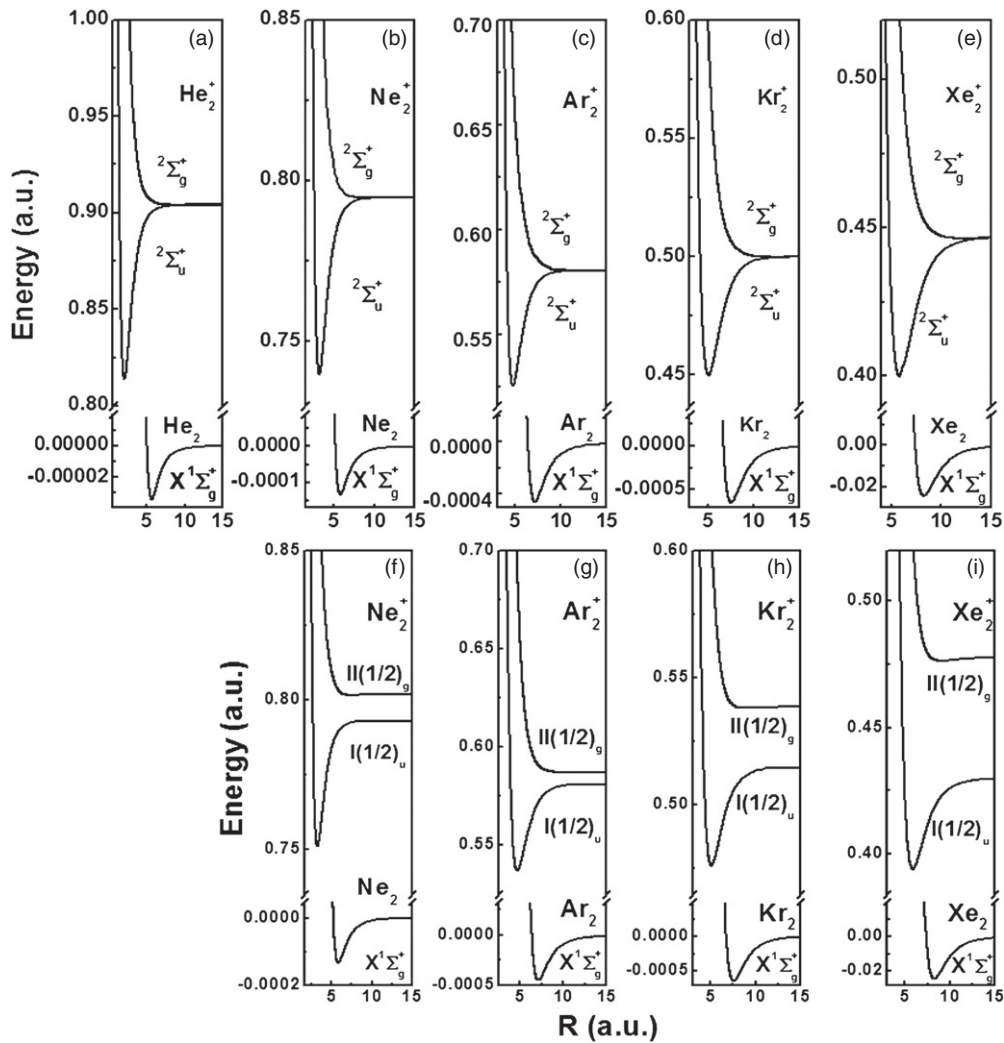


Figure 9. Adiabatic potential curves for the noble-gas dimer cations. (a)–(e) Potential curves for He_2^+ to Xe_2^+ without including spin–orbit coupling (no fine-structure splitting). (f)–(i) Potential curves for Ne_2^+ to Xe_2^+ including spin–orbit coupling (see footnote 3). Adapted with permission from [14]. © 2013, American Physical Society.

Figures 7(d) and (h) show the power spectra for 400 nm probe pulses and the corresponding field-dressed potential curves. Compared to the 800 nm spectra in figures 7(c) and (g) these power spectra differ substantially. For 800 nm probe pulses, most of the wave packet is trapped in the $a^4\Pi_u$ potential well, whereas for 400 nm probe pulses a significant portion of the nuclear probability density appears to be absent due to BS dissociation.

Figure 8 compares measured and calculated KER spectra as a function of pump–probe delay and QB frequencies for the $\text{O}_2^+ \rightarrow \text{O}^+ + \text{O}$ dissociation process with 10 fs width, 800 nm, $4 \times 10^{14} \text{ W cm}^{-2}$ peak intensity probe pulses. Details on measurements and calculations are given in [10, 11]. The KER spectra display energy bands separated by 0.1 eV and oscillations with a period of about 33 fs. The horizontal energy bands correspond to KERs from the vibrational energy levels of the $a^4\Pi_u$ adiabatic state starting from the $\nu = 10$ vibrational level that is energetically just above the dissociative limit of the $a^4\Pi_u$ and $f^4\Pi_g$ states. The oscillatory structure along the pump–probe delay axis is consistent with the wave-packet oscillation period in the $a^4\Pi_u$ state. The above observations

allow us to conclude that the $a^4\Pi_u$ and $f^4\Pi_g$ states are the main contributors in the O_2^+ dissociation dynamics. In addition to the main $4 \times 10^{14} \text{ W cm}^{-2}$ pulse, a weak $5 \times 10^{11} \text{ W cm}^{-2}$ pedestal with 100 fs pulse length was added in the numerical simulation to yield the energy-band structure. If no pedestal were added, this energy-dependent structure in the KER spectra would be absent.

Typically, several intermediate states contribute to the same KER. To identify electronic states that contribute to the experimentally-observed molecular dynamics, we derive the following scheme from the preceding discussion. We first calculate time-dependent probability density spectra and quantum-beat frequencies for each adiabatic molecular potential curve *independently* and compare respective calculated KER spectra—in both the time and QB frequency domain—with available experimental data, in order to assess the relevance of the selected adiabatic potential curve. Having identified the most relevant adiabatic electronic states, we include laser-induced dipole couplings between two (or more) preselected adiabatic electronic states and again compare the resulting KER spectra with experimental results. Should the

comparison not be satisfactory, we modify the set of relevant states, possibly including additional adiabatic states to the coupled-state calculation [10, 11].

3.3. Noble-gas dimers

In comparison to O_2 , noble-gas dimers feature a greatly reduced number of relevant adiabatic dimer cation states [13]. Figure 9 shows adiabatic potential curves of the noble-gas dimers without (panels a–e) and with (panels f–i) spin–orbit couplings (see footnote 3). Figure 10 exhibits probability densities and corresponding power spectra for the nuclear vibrational wave-packet propagation on the adiabatic $^2\Sigma_u^+$ potentials of the noble-gas dimer ions. The oscillation frequency, noticeable in the probability density spectra (left panels), decreases with the mass of the dimer. For heavier dimers, the wave packet moves more slowly on the $^2\Sigma_u^+$ state, resulting in larger oscillation periods. The number of oscillations completed before vibrational dephasing increases with the dimer mass and the quantum revival time are an order of magnitude larger for Xe_2^+ than for He_2^+ [13]. The QB frequencies are spaced more densely as the mass of the dimer increases (figures 10(b)–(j)). This is due to the fact that for heavier dimers the potential wells of the $^2\Sigma_u^+$ adiabatic potential curves are deeper and accommodate a larger number of vibrational states than in lighter dimers. The nuclear dynamics in laser-excited noble-gas dimer cations thus increasingly resembles classical nuclear motion for growing dimer mass.

Figure 11 summarizes the power spectra and corresponding field-dressed potential curves for Ne_2^+ in $10^{12} \text{ W cm}^{-2}$, 200 fs probe laser pulses with wavelengths of 1400 nm (figures 11(a) and (c)) and 800 nm (figures 11(b) and (d)). The outer classical turning points of the adiabatic field-dressed potential are mapped better for 800 nm pulses in figure 11(b) than for 1400 nm pulses (figure 11(a)), since the 800 nm BH well is deep enough to trap a significant part of the wave packet (cf figures 11(c) and (d)). For 800 nm wavelength pulses, the one-photon crossing appears at smaller internuclear distances than for 1400 nm pulses. Figures 11(c) and (d) indicate that the majority of the wave packet can be trapped by the BH well at internuclear distances between 4 and 7 au; this is corroborated by figures 11(a) and (b) as the majority of the wave packet yield is located in that same range.

Figure 12 summarizes the power spectra and corresponding field-dressed potential curves for Ar_2^+ in $10^{12} \text{ W cm}^{-2}$, 80 fs probe laser pulses with a wavelength of 1400 nm. The one-photon BH well is mapped comparatively better for $^2\Sigma_u^+$ and $^2\Sigma_g^+$ potential curves in figure 12(a) than the shallower BH well of the field-dressed $I(1/2)_u$ and $II(1/2)_g$ curves in figure 12(b).

To investigate the effect of fine-structure splitting on the nuclear motion we compare calculated power spectra $P(R, \omega, \tau)$ based on the adiabatic potential curves $I(1/2)_u$ and $II(1/2)_g$ including spin–orbit interactions with the results based on the adiabatic potential curves $^2\Sigma_u^+$ and $^2\Sigma_g^+$ that were computed without including spin–orbit interactions for Ar_2^+ (figure 12), Kr_2^+ (figure 13), and Xe_2^+ (figure 14). With increasing

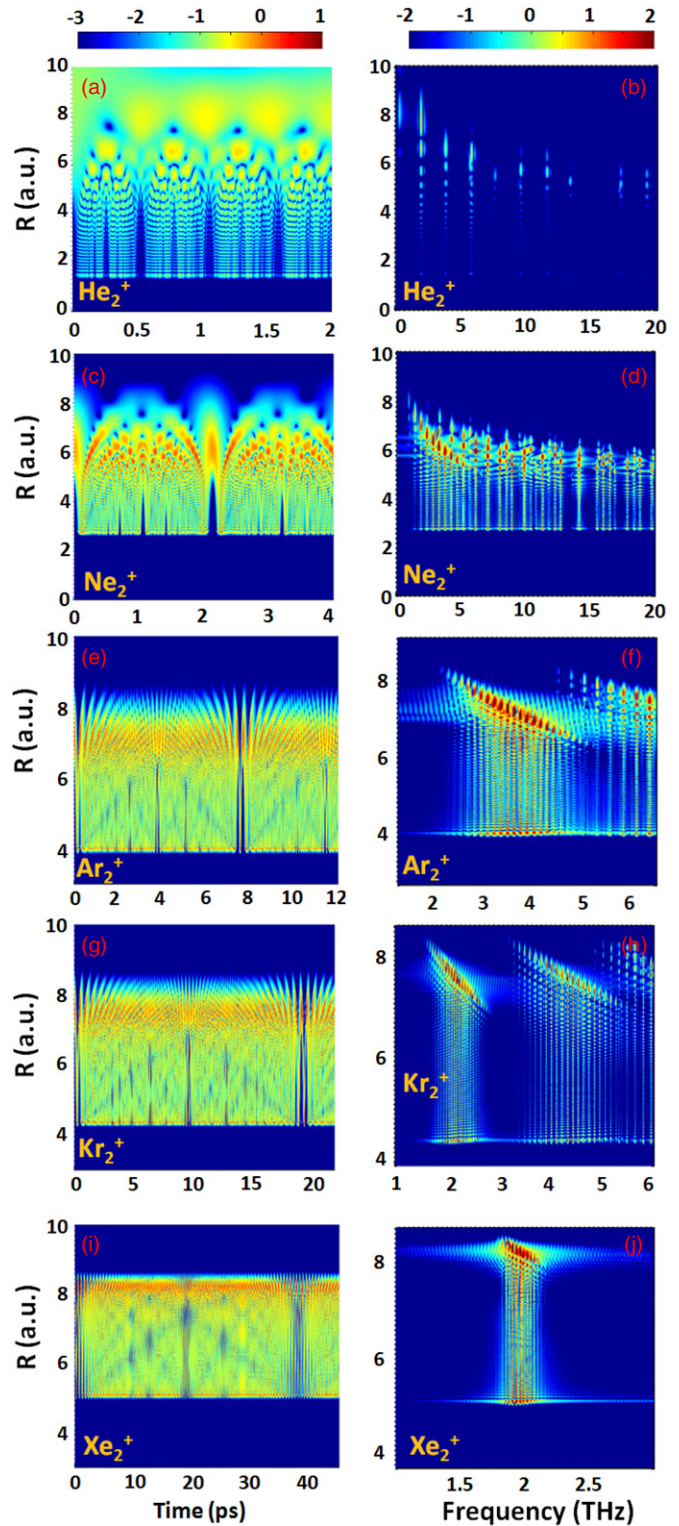


Figure 10. Nuclear probability densities (left) and corresponding power spectra (right) (logarithmic colour/greyscale) for the wave-packet propagation of nuclear vibrational wave packets on the adiabatic $^2\Sigma_u^+$ potential curves for (a), (b) He_2^+ , (c), (d) Ne_2^+ , (e), (f) Ar_2^+ , (g), (h) Kr_2^+ , and (i), (j) Xe_2^+ .

dimer mass, spin–orbit coupling becomes more relevant, and the $I(1/2)_u$ and $II(1/2)_g$ fine-structure splitting increases. This causes the BH well in Kr_2^+ (figure 13(d)) to become shallower than in Ar_2^+ (figure 12(d)). For the dipole-coupled

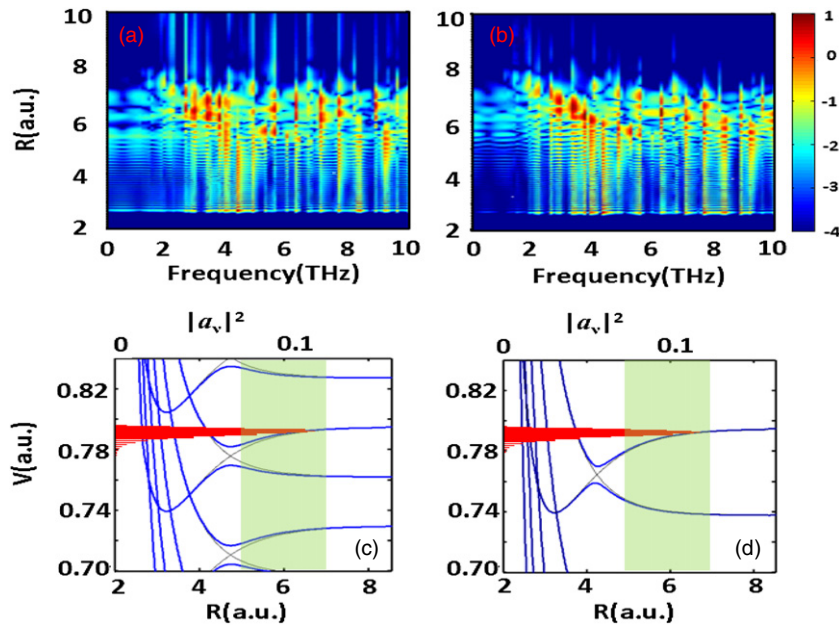


Figure 11. (a), (b) Power spectra (logarithmic colour/greyscale) and (c), (d) field-dressed potential curves for Ne_2^+ and 200 fs, $10^{12} \text{ W cm}^{-2}$ probe laser pulses with wavelengths of (a), (c) 1400 nm and (b), (d) 800 nm. Simulations based on dipole coupled $^2\Sigma_u^+$ and $^2\Sigma_g^+$ potential curves, not including fine-structure splitting. (c), (d) Field-dressed potential curves (thick blue curves) and corresponding field-free $^2\Sigma_u^+$ and $^2\Sigma_g^+$ adiabatic potential curves (thin black lines). Green-shaded areas indicate the FC region. Red horizontal lines show the FC probabilities $\{|a_\mu|^2\}$ at the corresponding stationary vibrational-state energies $\{\omega_\mu\}$.

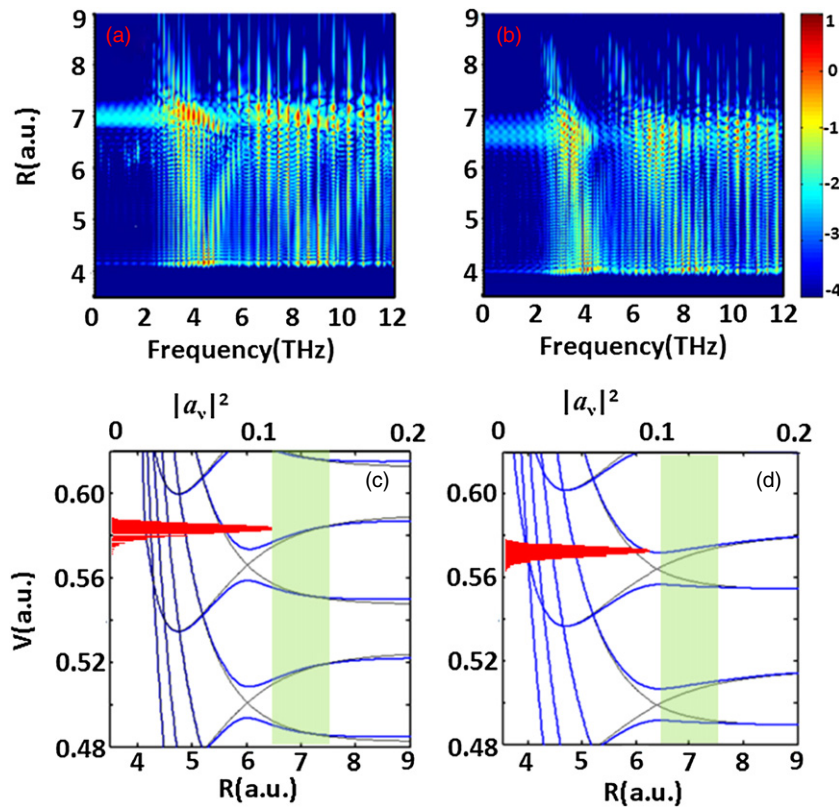
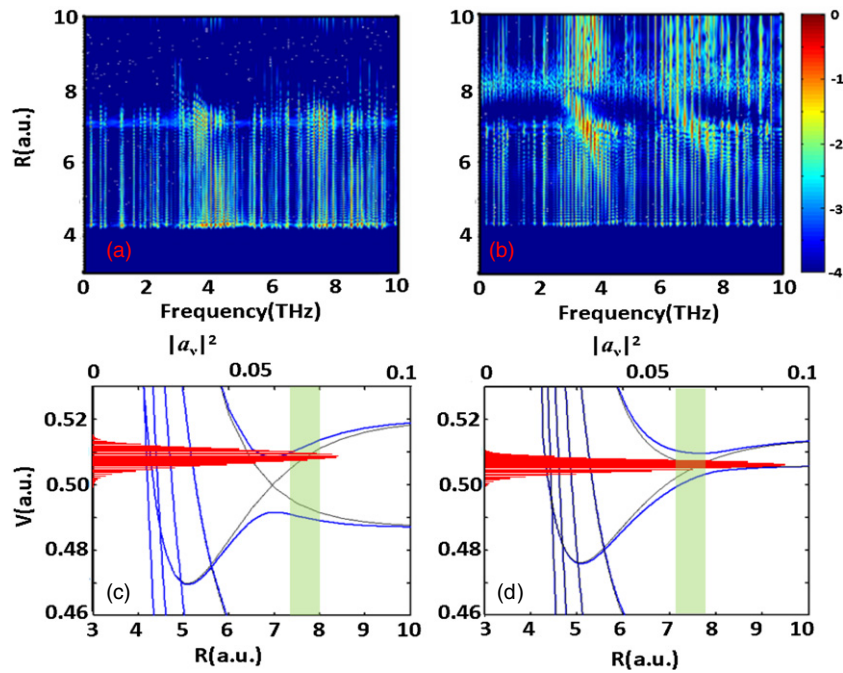
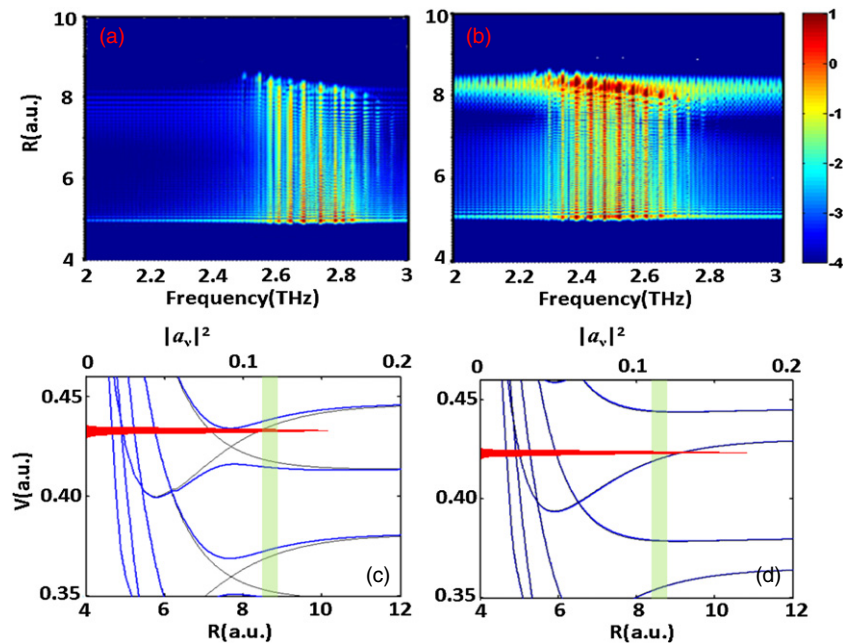


Figure 12. (a), (b) Power spectra (logarithmic colour/greyscale) and (c), (d) field-dressed potential curves for Ar_2^+ in 80 fs, $10^{12} \text{ W cm}^{-2}$, 1400 nm probe laser pulses. (a) Simulations based on dipole coupled $^2\Sigma_u^+$ and $^2\Sigma_g^+$ potential curves, not including fine-structure splitting. (b) Simulations based on the dipole-coupled $I(1/2)_u$ and $II(1/2)_g$ potential curves, including fine-structure splitting. (c) Field-dressed potential curves (thick blue curves) and corresponding field-free $^2\Sigma_u^+$ and $^2\Sigma_g^+$ potential curves (thin black lines). (d) Field-dressed potential curves (thick blue curves) and corresponding field-free $I(1/2)_u$ and $II(1/2)_g$ adiabatic potential curves (thin black lines). Green-shaded areas indicate the FC region. Red horizontal lines correspond to the FC probabilities $\{|a_\mu|^2\}$ at the corresponding stationary vibrational-state energies $\{\omega_\mu\}$.

Figure 13. Same as figure 12 for Kr_2^+ .Figure 14. Same as figure 13 for Xe_2^+ and 400 fs probe pulses.

$^2\Sigma_u^+$ and $^2\Sigma_g^+$ states, the BH wells for Ar_2^+ (figure 12(c)) and Kr_2^+ (figure 13(c)) are deeper compared to the $I(1/2)_u$ and $II(1/2)_g$ states (figures 12(d) and 13(d)). For Xe_2^+ , the fine-structure splitting exceeds the photon energy at 1400 nm and the $I(1/2)_u$ and $II(1/2)_g$ adiabatic potential curve one-photon crossings are absent (figure 14(d)).

4. Summary and outlook

We studied the bound and dissociative nuclear motion of vibrationally excited diatomic molecular ions in the time and frequency domains. While the time-domain KER spectra

display oscillation periods, revival times, and the nuclear-probability-density evolution, QB imaging in the frequency domain complements time-domain investigations of the nuclear dynamics by revealing (i) QB frequencies and the nodal structure of vibrational states within a given adiabatic molecular potential curve and (ii) laser-electric-field-dressed molecular potential curves. QB frequencies, wave-packet oscillation periods, and revival times are characteristics that indicate which adiabatic states of a photo-excited diatomic molecular ion are transiently populated during its bound or dissociative motion. Identifying these relevant potentials' curves by the combined analysis of experimentally-measured

KER spectra in the time and frequency domains, in comparison with simulated KER spectra, provides a powerful tool for analysing the nuclear dynamics in diatomic molecules and for identifying nuclear dissociation (and reaction) pathways. Due to the weak binding of noble-gas dimer cations and a small number of relevant electronic states, noble-gas dimers, in particular, are ideal targets for modelling the nuclear dissociation dynamics, allowing for the scrutiny of details such as the existence and relevance of transient BH states in field-dressed molecular potential curves. To identify states relevant in the dissociation dynamics, we discussed a scheme in which wave-packet propagation calculations are first performed separately for individual adiabatic potential curves, allowing for the selection of relevant adiabatic electronic states by identifying characteristic features (such as revival times, oscillation periods and quantum-beat frequencies) that the simulated time- and frequency-domain spectra have in common with measured KER spectra. Finally, after selecting the closest matches to the measured spectra, we carried out more complex calculations including the dipole coupling of these preselected states in the laser pulses. The QB imaging technique allows for the direct mapping of adiabatic nuclear potential curves and provides the distribution of stationary states that superimpose to form the nuclear vibrational wave packet that is launched by the molecular ionization in the pump pulse. In principle, this technique can be used to determine the internuclear-distance-dependent wavefunction of the nuclear wave packets (up to an overall phase) from measured KER spectra [8].

Acknowledgments

This work was supported by the National Science Foundation under grant no PHY-1068140 (KB), grant no PHY-1068752 (MM, UT), grant no PHY-1157044 (AK), and the Division of Chemical Sciences, Office of Basic Energy Sciences, Office of Science, US Department of Energy.

References

- [1] Ullrich J, Rudenko A and Moshhammer R 2012 *Annu. Rev. Phys. Chem.* **63** 635
- [2] Calvert C, Bryan W, Newell W and Williams I 2010 *Phys. Rep.* **491** 1
- [3] Ergler T, Rudenko A, Feuerstein B, Zrost K, Schröter C D, Moshhammer R and Ullrich J 2005 *Phys. Rev. Lett.* **95** 093001
- [4] Alnaser A S *et al* 2005 *Phys. Rev. A* **72** 030702(R)
- [5] Feuerstein B, Ergler T, Rudenko A, Zrost K, Schröter C D, Moshhammer R, Ullrich J, Niederhausen T and Thumm U 2007 *Phys. Rev. Lett.* **99** 153002
- [6] Winter M, Schmidt R and Thumm U 2008 *New J. Phys.* **12** 023020
Winter M, Schmidt R and Thumm U 2009 *Phys. Rev. A* **80** 031401 and references therein
- [7] Magrakvelidze M, He F, Niederhausen T, Litvinyuk I V and Thumm U 2009 *Phys. Rev. A* **79** 033410
- [8] Thumm U, Niederhausen T and Feuerstein B 2008 *Phys. Rev. A* **77** 063401
- [9] De S, Bocharova I A, Magrakvelidze M, Ray D, Cao W, Bergues B, Thumm U, Kling M F, Litvinyuk I V and Cocke C L 2010 *Phys. Rev. A* **82** 013408
- [10] De S *et al* 2011 *Phys. Rev. A* **84** 043410
- [11] Magrakvelidze M, Aikens C M and Thumm U 2012 *Phys. Rev. A* **86** 023402
- [12] Bocharova I A, Alnaser A S, Thumm U, Niederhausen T, Ray D, Cocke C L and Litvinyuk I V 2011 *Phys. Rev. A* **83** 013417
- [13] Wu J, Magrakvelidze M, Vredenburg A, Schmidt L, Ph H, Jahnke T, Czasch A, Dörner R and Thumm U 2013 *Phys. Rev. Lett.* **110** 033005 and references therein
- [14] Magrakvelidze M and Thumm U 2013 *Phys. Rev. A* **88** 013413
- [15] Jiang Y H *et al* 2010 *Phys. Rev. A* **82** 041403(R)
- [16] Magrakvelidze M *et al* 2012 *Phys. Rev. A* **86** 013415
- [17] Feldhaus J, Krikunova M, Meyer M, Möller T, Moshhammer R, Rudenko A, Tschentschler T and Ullrich J 2013 *J. Phys. B: At. Mol. Opt. Phys.* **46** 164002
- [18] Feuerstein B and Thumm U 2003 *Phys. Rev. A* **67** 063408
- [19] Ergler T, Rudenko A, Feuerstein B, Zrost K, Schröter C D, Moshhammer R and Ullrich J 2006 *Phys. Rev. Lett.* **97** 193001
- [20] Rudenko A, Ergler T, Feuerstein B, Zrost K, Schröter C D, Moshhammer R and Ullrich J 2006 *Chem. Phys.* **329** 193
- [20a] Rudenko A, Ergler T, Feuerstein B, Zrost K, Schröter C D, Moshhammer R and Ullrich J 2007 *J. Phys.: Conf. Ser.* **88** 012050
- [21] Robinett R W 2004 *Phys. Rep.* **392** 1
- [22] Marian C M, Marian R, Peyerimhoff S D, Hess B A, Buenker R J and Seger G 1982 *Mol. Phys.* **46** 779
- [23] Bransden B H and Joachain C J 2003 *Physics of Atoms and Molecules* 2nd edn (London: Prentice-Hall)
- [24] Feuerstein B and Thumm U 2003 *J. Phys. B: At. Mol. Opt. Phys.* **36** 707
- [25] Barone S R, Narcowich M A and Narcowich F J 1977 *Phys. Rev. A* **15** 1109
- [26] Bucksbaum P H, Zavriyev A, Muller H G and Schumacher D W 1990 *Phys. Rev. Lett.* **64** 1883